Tunnelling and Underground Space Technology 152 (2024) 105908

Contents lists available at ScienceDirect

Tunnelling and Underground Space Technology incorporating Trenchless Technology Research

journal homepage: www.elsevier.com/locate/tust

Real-time unsupervised monitoring of earth pressure balance shield-induced sinkholes in mixed-face ground conditions via convolutional variational autoencoders

Jorge Loy-Benitez [1], Hyun-Koo Lee [1], Myung Kyu Song, Je-Kyum Lee, Sean Seungwon Lee [*]

Department of Earth Resources and Environmental Engineering, Hanyang University, 222 Wangsimni-ro, Seongdong-gu, Seoul 04763, Republic of Korea

ARTICLE INFO

Keywords:
Autoencoders
Sinkhole formation
Earth pressure balance
Shield tunneling
Tunnel construction
Unsupervised monitoring

ABSTRACT

This study introduces a real-time unsupervised monitoring framework for monitoring sinkhole formation events during earth pressure balance (EPB) shield tunneling operations. A feature extractor (FE) is constructed by coupling variational Autoencoders structure with convolutional neural network layers (VAE-CNN) to manage the complexity of EPB operational data, including non-linearity and temporal dependencies. The monitoring framework consists of two main phases: offline modeling and online monitoring. In the offline modeling phase, an FE model is trained using data-intensive techniques to define a subspace characterizing the behavior of multivariate data without sinkhole formations. The squared prediction error (*SPE*) statistics and the control limits are computed for detection. During the online monitoring phase, unseen EPB data is propagated to generate *SPE* values and determine sinkhole events based on whether these values surpass the control limit. Sensor validity index violation counts were used to isolate the most influential variables, while the results demonstrated the superiority of the proposed VAE-CNN method, achieving a 100% detection rate and a 0.9% false alarm rate. The influential variables identified include cutter resolutions per minute, jack speed, screw pressure, torque, and cutter seal components. The monitoring system shows great potential for early warnings during EPB operations to mitigate sinkhole formation risks.

1. Introduction

The intensified urbanization and population growth witnessed in the past century have given rise to diverse urban needs, especially in urban infrastructure and effective transportation development. As cities expand, essential elements such as bridges, interchanges, roads, roundabouts, highways, and tunnels have become significant (Qiao and Huang, 2022). Tunneling, a significant process in transportation, strategic projects, and resource exploitation, has played a crucial role in advancements like subway transportation, hydroelectric plant construction, and underground mining (Pourhashemi et al., 2022).

With the rapid development of these infrastructures, tunnel boring machines (TBM) have been broadly utilized and preferred for tunnel construction due to their advantageous operations, as they execute closed-mode maneuvers that enhance safety measures by ensuring the stability of the surrounding rock mass (Huang et al., 2022). This involves utilizing instant support with concrete linings and mitigating the risks associated with groundwater pressure under the water table (Lee et al., 2021). Furthermore, shield tunneling operations are known for their efficiency, cost-effectiveness, and environmental friendliness (Ayawah et al., 2022).

Earth pressure balance (EPB) machines are shield TBM designed to function in soft ground conditions, water pressure, high water table, karstic, and sedimentary environments (Wan et al., 2024). During EPB

Abbreviations: AE, Autoencoders; *CNN*, Convolutional neural networks; *DR*, Detection rate; *EPB*, Earth pressure balance; *FAR*, False alarm rate; *H*, Hurst exponent; *KDE*, Kernel density estimator; *LSTM*, Long short-term memory; *MDR*, Misdetection rate; *PCA*, Principal component analysis; *PM*, Process monitoring; *RNN*, Recurrent neural networks; *R/S*, Rescaled range analysis; *SVI*, Sensor validity index; *SPE*, Squared prediction error; *t-SNE*, t-distributed stochastic neighbor embedding; *TBM*, Tunnel boring machine; *VAE*, Variational autoencoders; *ELBO*, Variational lower bound.

* Corresponding author at: Department of Earth Resources and Environmental Engineering, Hanyang University, 222 Wangsimni-ro, Seongdong-gu, Seoul 04763, Republic of Korea.

E-mail address: seanlee@hanyang.ac.kr (S.S. Lee).

[1] These authors contributed equally to this paper.

https://doi.org/10.1016/j.tust.2024.105908
Received 17 December 2023; Received in revised form 16 April 2024; Accepted 12 June 2024
Available online 27 June 2024

operations, geological variability introduces unexpected rock formations, structural configurations, and soil types, leading to a slower advance (Wang and Wang, 2020). The presence of mixed-faced and non-uniform ground conditions is particularly concerning, where soft soil in the upper layer combines with hard rock in the lower layer; moreover, face instability is prone to occur with soil arching collapse (Chen et al., 2024). These conditions jeopardize face support pressure and overall stability, increasing the risk issues such as excessive cutter wear, sinkhole occurrences, face collapse, and damage to nearby structures (Ko and Lee, 2020; Loy-Benitez et al., 2024a). Additionally, these disturbances might induce sinkholes, resulting in an active hazard to the surrounding infrastructures and traffic roads (Chen et al., 2023; Fang et al., 2020).

Sinkhole formation and ground settlements during EPB operations are inevitable and have been extensively investigated, resulting in numerous methods for predicting the effects of the tunneling process. Ground settlement troughs can be modeled by a *Gaussian* function, identifying the main cause of ground subsidence as stratum loss, defined by the difference between the volumes of the formed tunnel and excavated soil (Peck, 1969). However, due to the diverse conditions specific to tunneling projects, another study proposed variations to this model by modifying the width coefficient calculation to enhance adaptability (Attewell et al., 1986).

With the advent of machine learning (ML) algorithms, several investigations have focused on modeling ground subsidence using novel data-driven approaches. For instance, a random forest algorithm was applied to model ground settlements above the tunnel, using the maximum surface settlement value (S_{max}) and the trough width (i) as the ground surface settlement index; predictor variables included tunnel geometry, construction parameters, and geological properties (Zhou et al., 2017). Another study incorporated the general regression neural network (GRNN) to predict settlement, demonstrating superiority over other ML algorithms (Chen et al., 2019). Continuous monitoring and measurement during TBM operations enable real-time management processes. In this context, long short-term memory (LSTM) was introduced as a memory-based recurrent neural network (RNN) to exploit time-dependent features of continuous data collection and predict subsidence along the TBM drive (Lee et al., 2021). Similarly, Guo et al. (2022) exploited LSTM models to predict collapse areas based on torque and thrust force applied to non-collapsed areas (Guo et al., 2022).

These studies have predominantly used ML applications under a supervised learning framework, where the predicted variable is included in the dataset for regression or classification tasks. For subsidence prediction, a regression task is performed to indicate a settlement value; however, obtaining labeled data in cases with existing subsidence can be challenging in real-time monitoring due to operational constraints (Zhang et al., 2019). Therefore, a shift to an unsupervised framework aims to exploit the existing relationships among EPB process variables during operation, enabling the implementation of real-time monitoring techniques.

Unsupervised methods offer the flexibility to adapt to various ground deformation scenarios without requiring retraining the models when encountering different geological conditions. Process monitoring (PM) techniques guided by data-based, unsupervised methods have widespread applications in industrial, chemical, and environmental domains (Liu et al., 2018). These techniques have demonstrated different approaches within various fields, including fault diagnosis, fault isolation, fault reconciliation, and sensor validation, generally applied to a sensor network (Heloulou and Ramdani, 2014). These methods generally compare the actual behavior of the process with a model that represents the normal or desirable process behavior, exemplified as a subspace of important features conducted by data-intensive feature extraction and dimensionality reduction methodologies (Loy-Benitez et al., 2024b; Yan et al., 2016).

Principal component analysis (PCA) stands out among feature extraction methods as a state-of-the-art technique for PM. PCA extracts robust feature representations from high-dimensional process variables and transforms them into a few principal component variables (S. Brooks and Bauer, 2018). It involves a linear transformation onto a subspace where most features from the original variables are preserved while eliminating correlation to avoid redundancy (Navi et al., 2018). Nonetheless, the PCA model assumes that the original data satisfy the *Gaussian* distribution and are static, i.e., linear relationships without temporal dependencies, characteristics that are not present in real industrial processes.

With the development of ML algorithms, nonlinear methods for feature extraction in real-time monitoring have demonstrated superiority over state-of-the-art approaches, showcasing robustness in managing the complexity of analyzed processes. Autoencoders (AE) as neural network models equivalent to PCA shift the transformation function from linear to nonlinear, e.g., *Sigmoid*, *Tanh* and *ReLU*, being effective in handling real-world datasets (Rumelhart and Hintont, 2019). With the progress of generative modeling, several other approaches have been developed to handle other characteristics given the variant nature of data, including non-linearity and temporal-dependent features.

A prominent method is the variational autoencoders (VAE), which, unlike typical AE, works with a continuous latent space, where an inference model defines the encoder and the decoder is a generative model (Lee et al., 2019). Within these structures, utilizing fully connected layers is not ideal when dealing with dynamic information in the data. Therefore, a shift of layers is often conducted, replacing dense layers with RNN and memory-gated structures coping with seq2seq problems. Nevertheless, recent studies have shown that convolutional neural networks (CNN) outperform RNN in tasks such as audio synthesis and machine translation; moreover, Bai et al. (2018) concluded that CNN models can be considered as a first choice to solve seq2seq problems (Bai et al., 2018).

Operational data from the EPB are time series records, including penetration rate, muck volume, torque, thrust force, cutter head face pressure, thrust force, and chamber pressure. Given the temporal dependencies and non-linearity behavior of the data, linear approaches are unsuitable for digesting and modeling the data distribution. Therefore, this study suggests coupling VAE with CNN layers to exploit their capabilities in managing the non-linear temporal dependencies of operational EPB data.

This paper aims to develop an unsupervised framework for EPB-induced sinkholes via coupling VAE structures with Conv1D layers (VAE-CNN). The monitoring process utilizes real-time data from EPB operation to map meaningful representations onto a subspace that defines normal operation conditions, i.e., when a sinkhole formation is not registered. Then, unseen collected data can be mapped onto this subspace to detect sinkhole occurrences (Lee et al., 2019). The performance of the sinkhole formation detection is measured based on splitting the TBM data into training, probe, and test datasets, for which detection rate (*DR*), misdetection rate (*MDR*), and false alarm rate (*FAR*). This paper is structured as follows: Section 2 introduces the background for VAE and CNN, and Section 3 describes the collected data and the proposed monitoring framework. Section 4 presents the performance of the different techniques to detect EPB-induced sinkhole formation. Finally, the study conclusions are discussed in Section 5.

2. Convolutional variational autoencoders

This study introduces the incorporation of convolutional layers into the VAE structure for detecting sinkhole formation during operations, accounting for dynamic and non-linear data characteristics. The following subsections explain the structures and parameter optimization for CNN and VAE architectures.

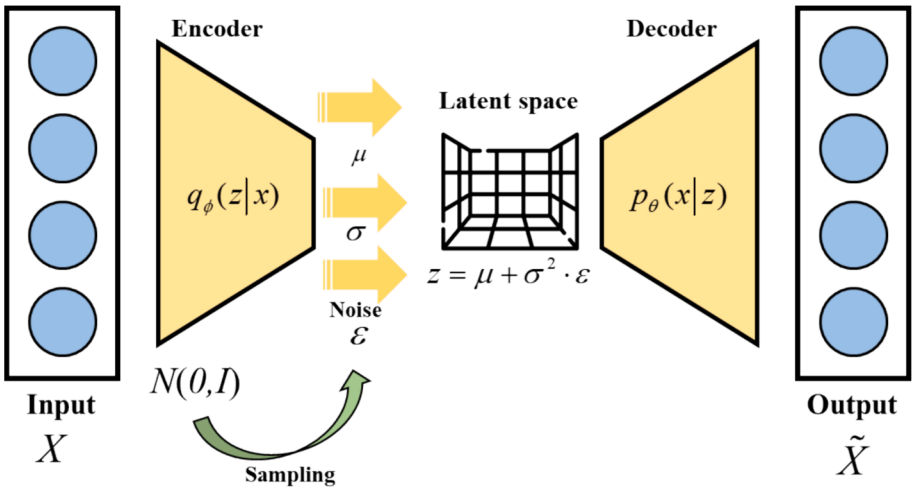

Fig. 1. VAE architecture.

2.1. Variational autoencoders

VAEs represent an alternative to the AE architecture, serving as generative models that couple Bayesian inference with deep neural networks. While AEs learn essential data representations by converting an input vector (X) into a lower-dimensional vector (z) and decompressing it for reconstruction, VAE learns the distribution of the latent representation space. The VAE structure comprises two main components, as shown in Fig. 1. The encoder $q_\phi(z|x)$ transforms the input (X) into a latent low-dimensional space, where ϕ represents the parameters for the encoder multilayered network. Simultaneously, the decoder $p_\theta(x|z)$ samples the latent space as an input and returns the parameters for a conditional distribution of the input X (Kingma and Welling, 2019).

Assuming that the input X is generated by an intrinsic distribution $p(x)$ represented by a latent variable z generated by a distribution $p(z)$, a joint distribution can be defined in **Eq. (1)**:

$$p(x,z) = p_\theta(x|z)p(z) \tag{1}$$

Here, $p(z)$ is the prior distribution of z, following a normal distribution with zero mean and unit variance and no parameters to be learned. The distribution of x given z is the likelihood $p_\theta(x|z)$, which simultaneously serves as the probabilistic decoder.

The optimal parameters for θ are obtained by maximizing the marginal likelihood explained in **Eq. (2)**.

$$p_\theta(x) = \int p(z)p_\theta(x|z)dz \tag{2}$$

Nevertheless, the maximization of the marginal likelihood represents an unmanageable process, as it is not possible to exhaust the latent variable. To address this problem, the likelihood $\log p_\theta(x)$ is represented in **Eq. (3)** (Zhang et al., 2019).

$$\log p_\theta(x) = E_{q_\phi(z|x)}[\log p_\theta(x|z)] - D_{KL}(q_\phi(z|x)\|p(z)) + D_{KL}(q_\phi(z|x)\|p_\theta(z|x)) \tag{3}$$

Both the probabilistic encoder and decoder are included, $D_{KL}(A\|B)$ represents the Kullback-Leibler divergence (*KLD*), describing the agreement between two distributions A and B (Guo et al., 2020). The divergence is defined as follows:

$$D_{KL}(A\|B) = \int_{-\infty}^{\infty} a(x)\log\frac{a(x)}{b(x)}dx \tag{4}$$

Here, a and b are the probability densities of A and B, respectively. Considering that *KLD* yields non-negative expressions; the third term of **Eq. (3)** can be neglected when maximizing the log-likelihood of the marginal distribution. This results in a variational lower bound (*ELBO*), which is considered a loss function $\ell(\bullet)$ explained in **Eq. (5)** (Zhang et al., 2019).

$$\ell(\phi,\theta;x) = E_{q_\phi(z|x)}[\log p_\theta(x|z)] - D_{KL}(q_\phi(z|x)\|p(z)) \tag{5}$$

The parameters ϕ and θ for the encoder and decoder, respectively, are optimized by maximizing the *ELBO*, which is equivalent to minimizing the reconstruction error of a standard AE (Kingma and Welling, 2019).

2.2. Convolutional neural networks

Contrary to traditional neural networks, CNN models employ convolutional operations followed by a pooling process instead of general matrix multiplication (Kalchbrenner et al., 2014). Time series are one-dimensional grids sampled at regular intervals and can be effectively processed using one-dimensional convolutional layers (Conv1D). Given an input X , the network learns a set of parameters Ω to generate a reconstruction $\widehat{X}$ through a hierarchical feature extraction, as computed in **Eq. (6)**.

$$\widehat{X} = F(X|\Omega) = f_S(\ldots f_2(f_1(X|\Omega_1)|\Omega_2)|\Omega_S) \tag{6}$$

Here, S is the number of hidden layers; then, the operation for the s^{th} layer is computed as follows:

$$\widehat{X}_s = f_s(X_s|\Omega_s) = \sigma(W \otimes X_s + b), \Omega_s = [W,b] \tag{7}$$

X_s represents a two-dimensional input matrix with N feature maps, W represents a set of N one-dimensional kernels and b is a bias vector. The activation function is denoted by $\sigma(\bullet)$ and $\otimes$ is a convolutional operation. Additionally, pooling layers increase the area covered by the next fields and finally, the output from the convolutional layers is flattened for use as inputs in fully connected layers.

3. Materials and methods

3.1. Project description and earth pressure balance tunnel boring machine driving

The data for EPB-type TBM were obtained from a metropolitan project in downtown Seoul. The tunnel is 1,600 m long and has two stations and seven ventilation shafts. The alignment lengths were 760 m and 762 m for the northern and southern tunnels, respectively, with a total installation of 1,011 segment rings. A single EPB TBM was used for excavating single-track twin tunnels, resulting in a total excavation

Table 1
Characteristics of the EPB-TBM.

Item	Description
Type	Earth pressure balance
Supplier	Hitachi Zosen (Japan)
OD/ID	7.69 m/7.47 *m*
Thrust force	1,120 kN/m^2/52,000 kN
Cutter head	Dome type, 17-inch cutter, scraper
Torque	11,300 – 4,3300 kN-m ($\alpha = 24.8$)
RPM	0.6—3.53 RPM, electric motor type
Segment	RC-segment, L 1,500 mm + t 300 mm, 7 pieces
Muck handling	Muck car + vertical conveyor belt, belt scale
Grouting	Upper Section 4EA, Lower section 2EA, Chamber 4EA

Table 2
Tunneling project geological conditions.

Item	Rock characteristics
Residual soil	Sandy gravel, N: 3—50, max size: φ500 mm
Weathered rock	Silty core, Cohesion: 31 kPa, $\varphi = 32^{\circ}$
Soft rock	Gneiss, RMR: 30—50
Water Level	Approx. GL-7 *m*
Unit weight	20 – 21 kN/m^2
UCS	20—110 MPa
Permeability	$2.5 \times 10^{-3} - 2.5 \times 10^{-5}$ cm/s

length of 1,522 m. The tunnel was relatively shallow, at approximately 6 to 20 m, and the ground composition at the departure zone consisted of a mix of weathered and soft rock, whereas the arrival zone comprised alluvial soil. The groundwater level was approximately 7 to 8 m below the surface and 3 to 4 m above the tunnel crown. Table 1 outlines the dimensions and specifications of the EPB TBM used in the project.

In addition, Table 2 contains relevant information on the geological conditions along the tunnel alignment, while Fig. 2 illustrates the geological layout of this alignment. The main characteristic of the site is that at the tunnel depth, the geology consists of a mixed-faced condition with alluvial gravel at the crown, weathered rock in the middle, and soft to hard rock at the bottom of the tunnel face. A mixed-face condition is unfavorable for face stability, increasing the risk of settlements due to over-excavation at the crown, while the bottom section represents a delay in the construction of the tunnel.

3.2. Data description, split, and preliminary analyses

The EPB dataset comprises 42 operational variables collected in defined cycles known as rings. The observations are collected with a time resolution of 2–3 min, and for each ring, 75–80 instances can be collected. Operational features are listed in **Table S1 supplementary information (SI)**. A total of 104 rings are marked as non-sinkhole events occurring, while six rings are marked as sinkhole events occurring. For the development of this investigation, the feature extraction method necessitates data under normal conditions, i.e., non-sinkhole event occurrence. In contrast, data with abnormal conditions should be introduced for testing this method, i.e., sinkhole event occurrence.

The total EPB operational data is divided into three datasets**.** Non-sinkhole occurring events observations account for 6,400 instances and they are divided into two parts in a proportion of 90/10, the training (5760 observations) and probe (640 observations) sets, for training the feature extraction model and validating the model, respectively. On the other hand, the test data (1536 observations) consists of sinkhole-occurring events to test the trained model.

Additionally, this study presents the coupling of two neural models that are well known for their performance on data with temporal dependencies and non-linear distributions. To assess these characteristics, the Hurst exponent (H) is evaluated, a parameter in [0,1], and indicates long temporal independence among the observations. H is estimated through rescaled range analysis (R/S) with a regression explained in **Eq. (8)** (Lotfalinezhad and Maleki, 2020; Mandelbrot and Wallis, 1969).

$$\log(R/S)_n = \log c + H \log n \tag{8}$$

Here, S is the standard deviation, R is the range, n is the subseries length, and c represents a positive constant. This parameter denotes a series Brownian motion or independence; for instance, $H = 0.5$ indicates that the given series follows a Brownian motion or refers to independence; on the other hand, a variation of this value represents dependence on past values, when $H \in (0.5, 1]$, the series is considered persistent, or when $H \in (0, 0.5)$, the series is considered anti-persistent (Ba-Alawi et al., 2021).

3.3. Sinkhole occurrence detection and feature identification

In the PM context, several feature extraction methods have been used to detect, identify and reconstruct abnormal events and sensor failures (Loy-Benitez et al., 2023). This section describes high-dimensional feature extraction techniques for abnormal event detection and isolation in an online monitoring schema.

3.3.1. Sinkhole occurrence detection

Multivariate high-dimensional PM techniques have evolved with technological advances, transitioning from statistical to neural methods. However, they share a common logic, i.e., they project the multivariate normal operation dataset of a process onto a latent low-dimensional space that extracts relevant information from the process (Lee et al., 2019). Based on this projection, multivariate control charts are derived to determine whether new observations are under control or follow

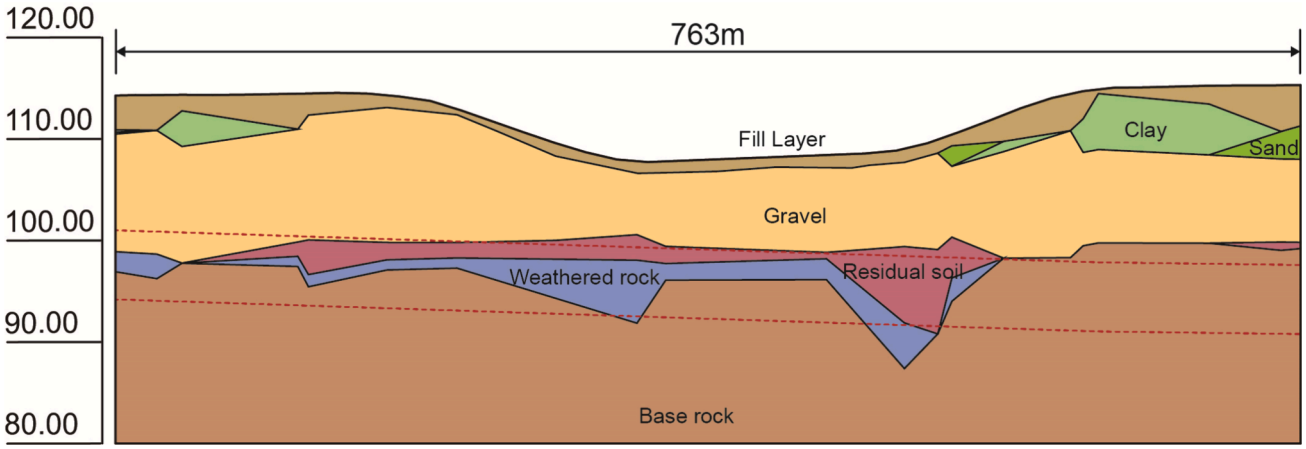

Fig. 2. Layout of the geological conditions along the tunnel alignment.

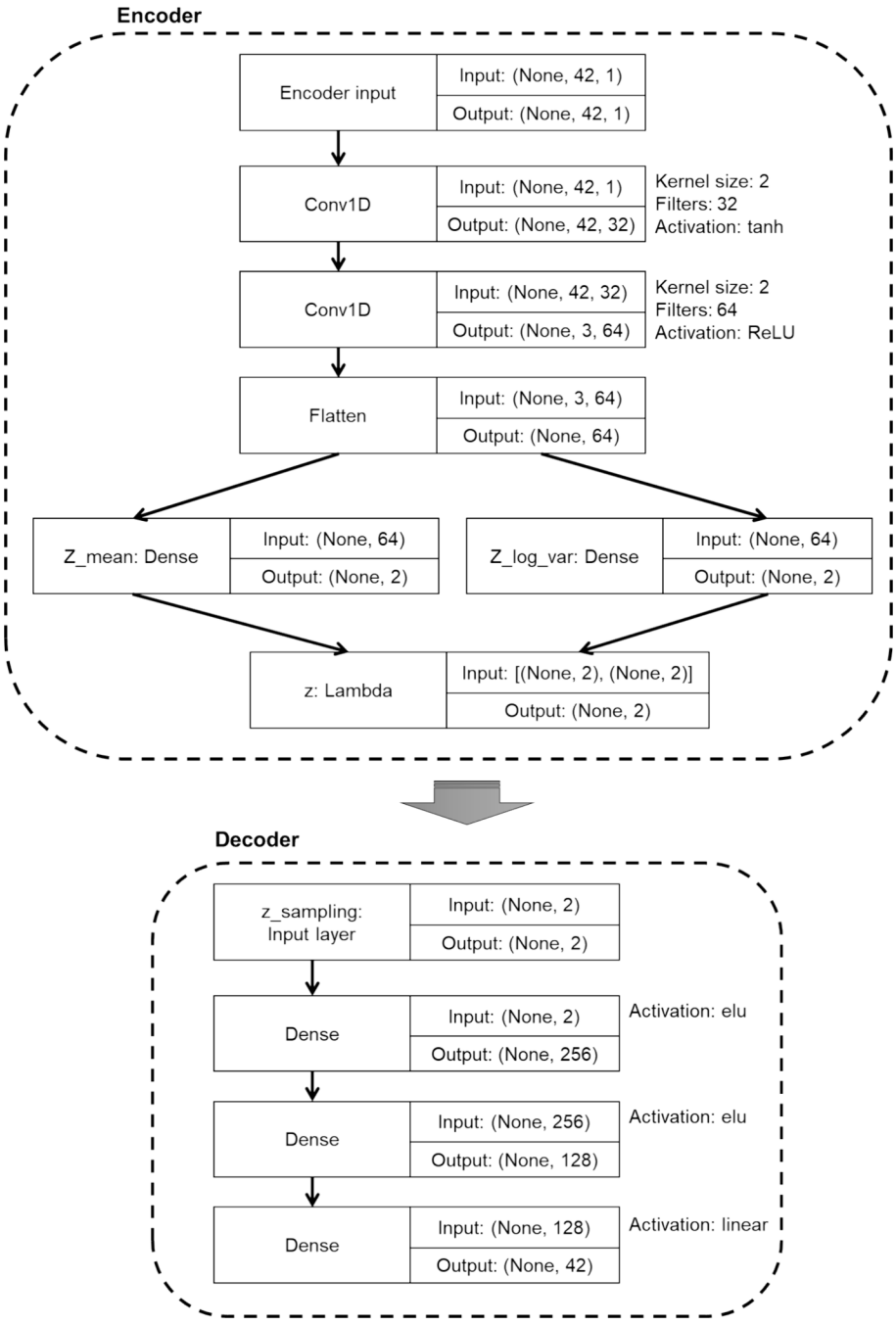

Fig. 3. The implemented VAE-CNN model for training the sinkhole event detection.

desirable process conditions (Ku et al., 1995).

This study proposes a VAE-CNN structure for real-time sinkhole formation detection during EPB operation. Considering that the probabilistic decoder $p_\theta(x|z)$ outputs a distribution of x given z; different samples can be drawn from $N(\mu, \sigma)$ with expected value μ. The monitoring statistic utilised is the Q statistic, also known as the squared prediction error (*SPE*), established in the residual subspace (Yan et al., 2016). When new observations are propagated through the VAE-CNN and projected onto the residual subspace, falling below the *SPE* limits are considered normal observations; otherwise, they are characterized as abnormal.

In this case, the VAE-CNN model is trained with EPB operational data in which no sinkhole occurrence has been registered, i.e., training data. Then, a statistical model is constructed by defining the monitoring statistics. Once this is defined, statistics for the operational data with sinkhole occurrences can be computed, and abnormal events can be detected according to the control limits. The *SPE* statistic is computed based on the reconstruction error (e) between input X and reconstruction $\widetilde{X}$. The *SPE* is explained in **Eq. (9)** and reflects the noise information of all the process variables.

$$SPE = e^T e = \left(X - \widetilde{X}\right)^T \left(X - \widetilde{X}\right) \tag{9}$$

After computing the *SPE* statistics, defining control limits is essential to detect whether new observations differ from normal EPB operations, indicating a sinkhole occurrence. The representations in neural feature extraction methods do not follow *Gaussian* distributions. Consequently, control limits cannot be determined via the distribution of statistics, such as in PCA; therefore, the control limit is established using kernel

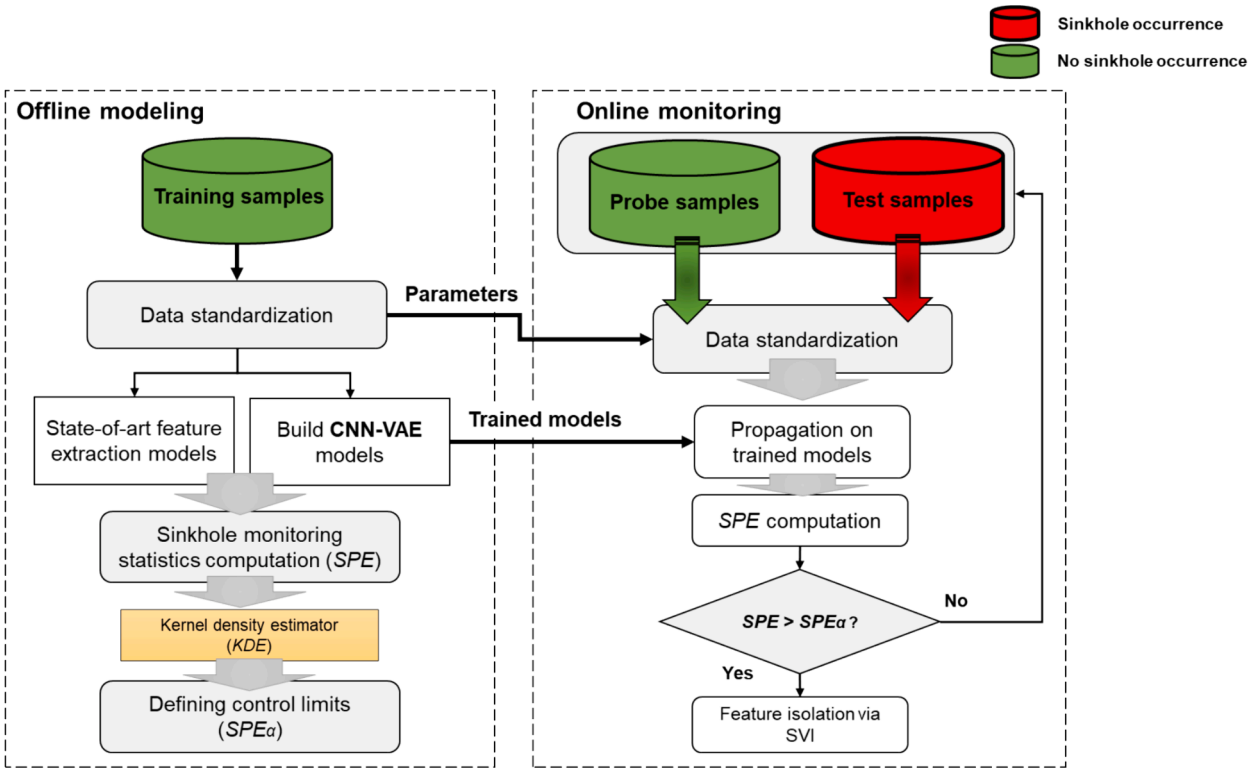

Fig. 4. The research framework for the detection and isolation of sinkhole formation during EPB operation.

density estimation (KDE), which estimates the probability density function of a random variable (Lee et al., 2004). The KDE first assumes that the observations are generated by an unknown probability density; then, it fits the probability density of the data with a density estimator $g(x)$.

Considering that the process data $[x_1, x_2, \ldots, x_n]$ is generated by some distribution with an unknown probability density function $g(x)$, where the data is independent and identically distributed. To determine the form of the function $g(\bullet)$, a kernel density estimator is computed as explained in **Eq. (10)**.

$$g(x) = \frac{1}{m}\sum_{j=1}^{m} K_h(x - x_j) = \frac{1}{m\sigma}\sum_{i=1}^{m} K\left(\frac{x - x_j}{\sigma}\right) \tag{10}$$

Here, x is the data point under consideration, x_j represents an observation from the dataset, m is the number of observations, K is the kernel function, and σ is the window width. This computation allows estimating of normal *SPE* values, i.e., when no sinkhole occurs during the EPB operation. The control limit SPE_α is obtained by taking the α quantile from its density estimator, where α represents the significance level, and in this case, $\alpha = 0.05$, indicating a confidence level of 95 %.

3.3.2. Sinkhole occurrence feature isolation

In general, once an abnormal event is detected within a monitored process, sensor isolation is a necessary step to identify potential features that might represent responsibility on the sensor network failure. In this study, the abnormal event is detected through deviations in the measurements of the EPB operational data; however, sinkhole formations cannot be attributed to sensor malfunction as they are not the cause of these events. Then, an isolation method is presented for identifying those sensors that require the most attention when generating information or indicating the sinkhole formation process.

Conventionally, the sensor validity index (*SVI*) is commonly utilized to identify faulty sensors within the sensor network (Kim et al., 2013). This index corresponds to the ratio between the *SPE* vectors obtained during the abnormal event detection process, as defined in **Eq. (11)**.

$$SVI_j = \frac{SPE\left(x_j^*\right)}{SPE(x)} \tag{11}$$

Here, $SPE(x)$ represents the *SPE* vector of the original sample vector x, while $SPE\left(x_j^*\right)$ is the *SPE* vector of the reconstructed vector and j is the number of features. The impact of each variable is measured by the rate, and when the i^{th} sensor evidences a large impact while $i \neq j$, the reconstructed vector x_j^* contains this impactful sensor as the $SPE\left(x_j^*\right)$ will not show a significant reduction. On the contrary, when the impactful sensor is correctly identified, i.e., $i = j$, a large reduction $SPE\left(x_j^*\right)$ is anticipated. In this case, the ratio shown in *SVI* is more sensitive (Wang and Chen, 2004).

Finally, a visual representation of the different conditions of sinkhole occurrence can be obtained utilizing scatter plots of principal components obtained from linear transformations onto a subspace. In this study, the residual yielded by the proposed method corresponds to a high-dimensional array ($n = 42$); the visualization is conducted through the t-distributed stochastic neighbor embedding (t-SNE) (Laurens van der Maaten and Hinton, 2008).

3.4. VAE-CNN model training

The selected model for monitoring sinkhole occurrences is the coupled VAE-CNN. In unsupervised monitoring, the selected method generates a subspace to be subsequently reconstructed (Gondara and Wang, 2018). For model training, the input and output layers have the same dimension, comprised by 42 neurons representing the number of EPB operational data features. The proposed model encodes the input X as a distribution onto the latent space from which an observation is sampled and finally decoded into the output $\widetilde{X}$.

Fig. 3 depicts the implemented VAE-CNN core structure with its corresponding dimensions and main parameters. The encoder comprises

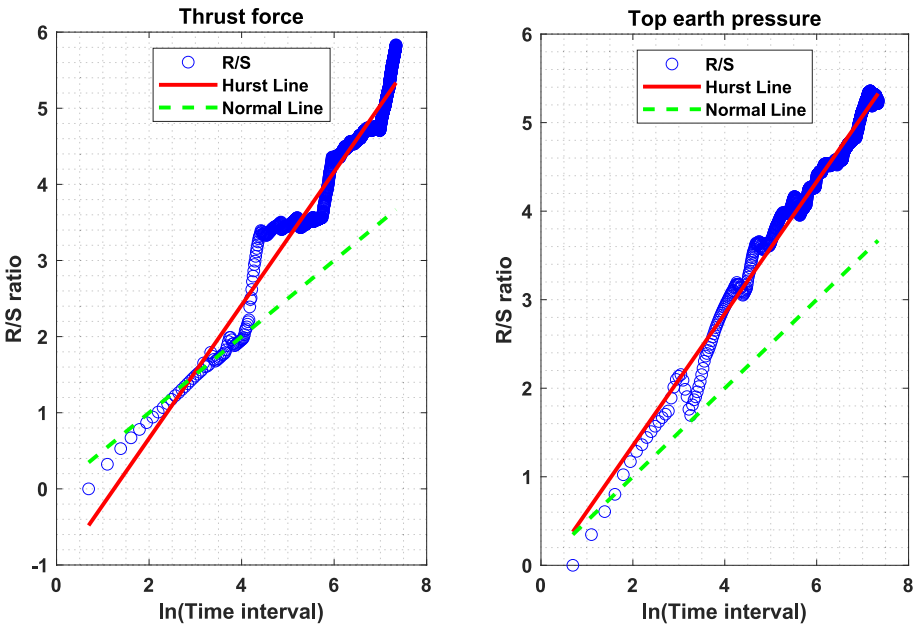

(a) (b)

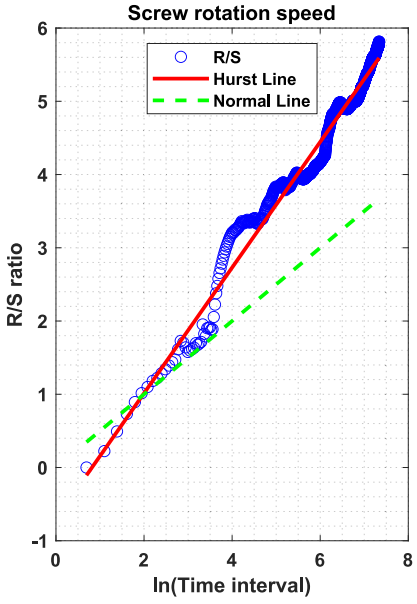

(c)

Fig. 5. Variations of R/S analysis for Hurst exponent determination for (a) thrust force, (b) top earth pressure, (c) screw rotation speed, and (d) Hurst exponent for each EPB variable.

two stacked Conv1D layers with a common Kernel size of two, using 32 and 64 filters, and employing the *tanh* and ReLU activation functions, respectively. In addition, a Dense layer generates the mean and log-variance to simplify the loss function computation. The second part is the decoder, which receives the output from the encoder, i.e. the sampling from the latent space z. The decoder comprises two stacked Dense layers with 256 and 128 neurons. The activation function for these two layers is *elu*, and the output layer is a Dense layer with 42 neurons and linear activation. This generated reconstruction is approximately similar to the inputs.

Computationally, the Deep Learning library Keras is utilized with 500 epochs and a batch size of 72. The optimization is conducted using the Adam optimizer. The computation is operated on a system with the following characteristics: 13th Gen Intel® Core™ i9-13900 K @ 3.00

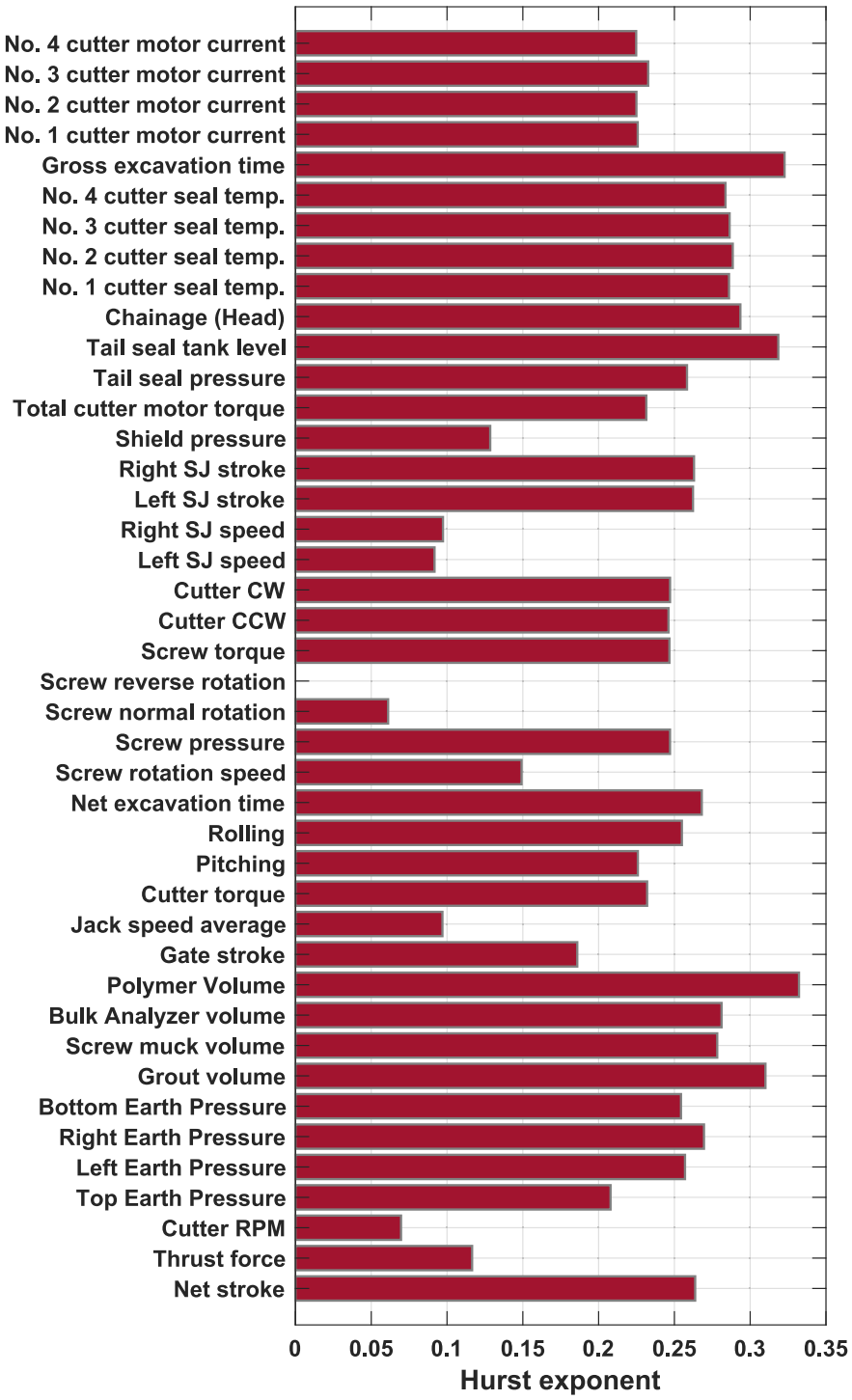

(d)

Fig. 5. (*continued*).

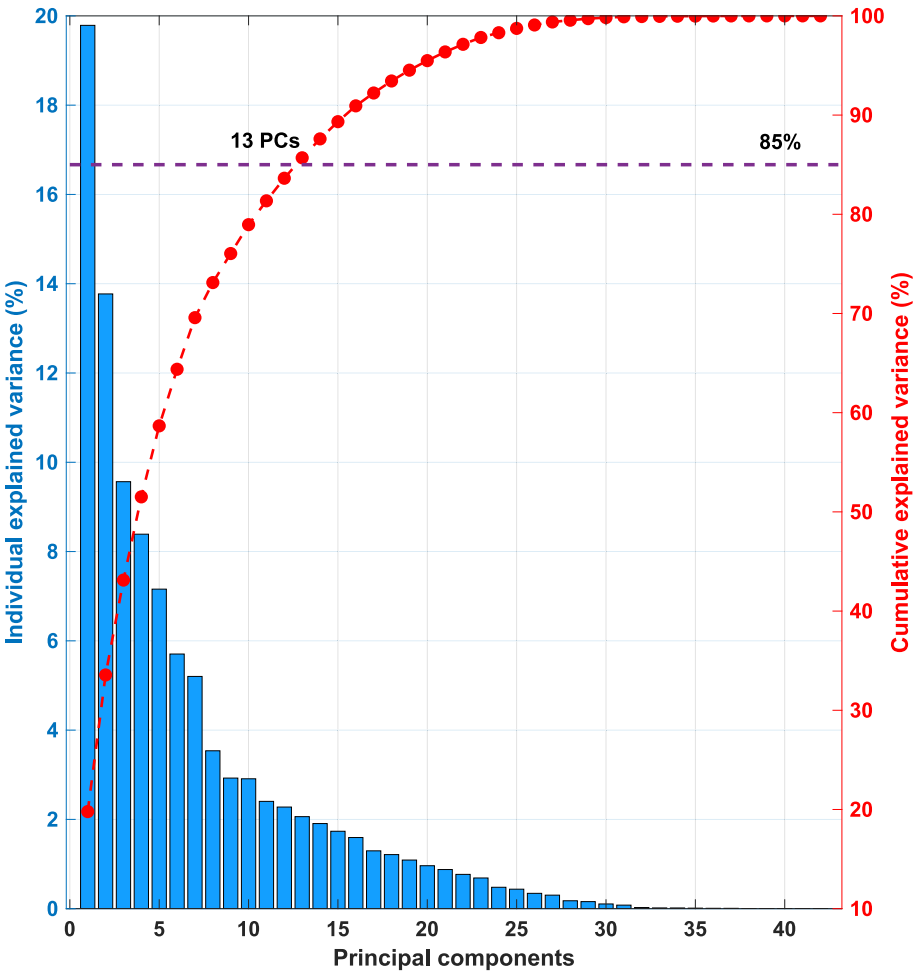

(a)

Fig. 6. Evaluation of EPB operational data via PCA using (a) explained variance and (b) variable vectors.

GHz, 32.0 GB RAM and x64-based processor.

3.5. The proposed method

The real-time monitoring method for sinkhole formation during the EPB operation is defined by two main phases, illustrated in Fig. 4. These phases are described as follows:

- *Offline modeling*:

(1) Collect the EPB operational data training set
(2) Standardise each feature with zero mean and unit variance, save parameters
(3) Train the VAE-CNN model
(4) Compute the monitoring statistic *SPE* with its corresponding control limits using *KDE* with a significance level of 0.05

- *Online monitoring*:

(1) Collect probe and test datasets and standardize them with the training set parameters
(2) Propagate the standardized data through the trained VAE-CNN model to obtain the reconstruction
(3) Compute the monitoring statistic *SPE* and compare these observations with the defined control limit SPE_{α}.
(4) Calculate the *SVI* to evaluate how important each sensor is on the event occurrence in terms of counting the times the observed values located below the control limit $SVI_{lim} = 0.5$.

Several state-of-the-art feature extraction models are trained, including PCA, independent component analysis (ICA), dynamic independent component analysis (DICA), Kernel PCA (KPCA), AE, Stacked AE and VAE to compare and select the most suitable method for detecting sinkhole occurrence events. For the fairness of the analysis, the PCA and KPCA methods are trained with 13 principal components.

The performance of the proposed method is evaluated using different metrics. For instance, when evaluating probe samples in which no sinkhole occurrence is recorded, the *SPE* values are expected to fall below the respective control limit. However, when an abnormal observation is detected, it can be attributed to a false alarm occurrence. A false positive (*FP*) value indicates the instances in which a sinkhole formation is detected when it is not actually registered; moreover, a true negative (*TN*) value indicates the instances in which a sinkhole occurrence is not detected and not registered. The *FAR* metric is explained in **Eq.** (12).

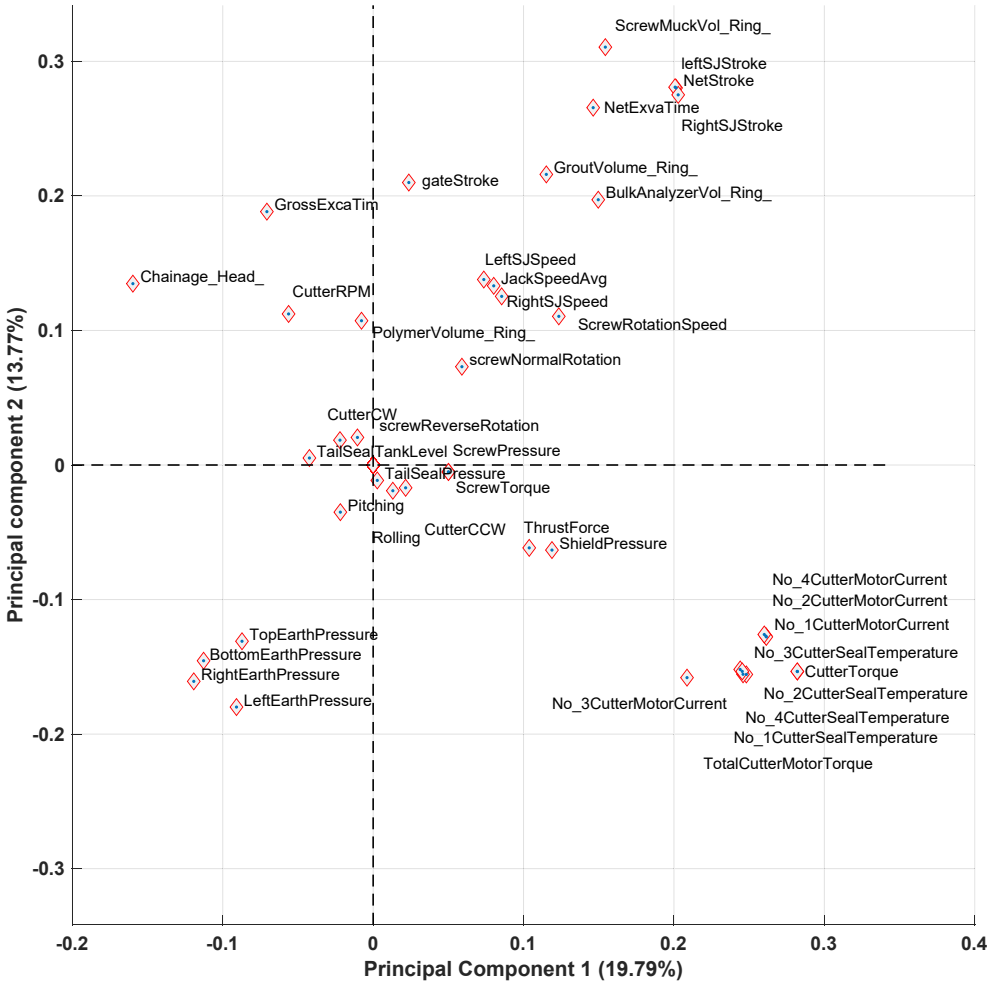

(b)

Fig. 6. (*continued*).

$$FAR(\%) = \frac{FP}{FP + TN} \times 100 \tag{12}$$

On the other hand, when propagating the test samples, as all these values are observations where sinkhole events occur, it is expected that all the *SPE* measurements surpass the control limit. Therefore, two metrics can be computed to evaluate the accuracy of the proposed method. The detection rate (*DR*) is a metric that quantifies the ratio between the detected abnormal events and the total abnormal events registered in the observations, as described in Eq. (13).

$$DR\ (\%) = \frac{\text{Number of detected sinkhole occurrences}}{\text{Total number of actual sinkhole occurrences}} \times 100 \tag{13}$$

Moreover, the misdetection rate (*MDR*) is the ratio of misdetected sinkhole event occurrences to the total number of the sinkhole occurrence registered in the observations, as explained in Eq. (14).

$$MDR\ (\%) = \frac{\text{Number of misdetected sinkhole occurrences}}{\text{Total number of actual sinkhole occurrences}} \times 100 \tag{14}$$

4. Results and discussion

4.1. Preliminary operational earth pressure balance shield data analysis

The proposed monitoring method for sinkhole occurrences incorporates a neural structure as a feature extractor, effectively managing non-linear relationships and temporal dependencies. A preliminary data analysis was conducted to assess the pertinence of the applied methods. In this context, the Hurst exponent for the EPB data features was determined. Fig. 5**(a) – (c)** corresponds to the relationship between the R/S and the time interval for the thrust force, top earth pressure variables, and screw rotation speed, respectively. In these figures, the red line indicates the Hurst line as a fitting for the R/S tendency, representing the trend given from each feature, while the dashed line corresponds to the normal line, which indicates normal behavior. If the R/S points of an analyzed variable coincide with the normal line, it means that H is equal to 0.5, indicating that the time series follows a Brownian motion and behaves as a Gaussian noise with a normal distribution without long memory (Hernán et al., 2015). For these three variables, it can be observed that none of the Hurst lines obey the normal line and, therefore, can be considered far from normality.

In addition, Fig. 5**(d)** illustrates the magnitude of H for all the EPB operation variables in the analysis. It is observed that all these values will fall below the threshold ($H = 0.5$), at which the series is considered to exhibit Brownian motion or independent temporal dependencies. The Hurst index for all the operational variables exhibits $H < 0.5$, indicating that the time series of the EPB operation variables represent an anti-persistent motion. In this context, there is a high probability that an increasing value at time t can be decreased by time $t + 1$, and conversely, if a low value is observed at time t, an increasing value can be observed by time $t + 1$ (Lotfalinezhad and Maleki, 2020). This behavior is

Table 3
Sinkhole event detection performance for the different introduced methods.

Method	Probe set	Test set	
	False alarm rate (%)	Detection rate (%)	Miss detection rate (%)
PCA	12.8	98.8	1.2
ICA	11.9	100.0	0.0
DICA	5.5	100.0	0.0
KPCA	2.3	100.0	0.0
AE	11.3	99.2	0.8
StackedAE	1.6	100.0	0.0
VAE	1.6	99.1	0.9
VAE-CNN	**0.9**	**100.0**	**0.0**

appropriate for cyclic measurements, with the series being collected as different defined rings that are concatenated to generate the operational time series.

Additionally, PCA is utilized to explore the relationships among the EPB data variables. Fig. 6**(a)** shows the individual explained variance for each variable, while the threshold is set to maintain 85 % of the eigenspectrum. Consequently, 13 principal components were identified to explain the desired variance. On the other hand, Fig. 6**(b)** depicts the biplot yielded by the variables, where each marker represents the vector ends. The markers positioned further from the origin signify a greater contribution to the principal components. In this instance, it can be observed that variables such as net stroke and cutter-related variables, including torque, seal temperature and motor current exhibit great magnitudes corresponding to their contribution to the variance.

In the analyzed data for this case study, the position and angles between the variable vectors reveal the degree of correlation. Closely correlated variables form notable clusters; for instance, cutter-related variables share a strong correlation in the second quadrant, screw-related variables in the first quadrant, and earth pressure variables in the third quadrant. Furthermore, when forming a 90-degree angle with other vectors, non-correlation is observed in variables located in subsequent quadrants, such as net stroke and cutter seal temperatures. Conversely, forming a 180-degree angle indicates a negative correlation, as seen in relationships such as net excavation time and earth pressures or thrust force and cutter rotational speed (RPM).

For instance, the relationship between thrust force and cutter RPM evidences a negative correlation as they are located on opposite sides with respect to the origin. Operationally, depending on the geological conditions where the EPB is excavating, with dense soils, high torque is needed, while the rotation slows down due to the resistance found by the

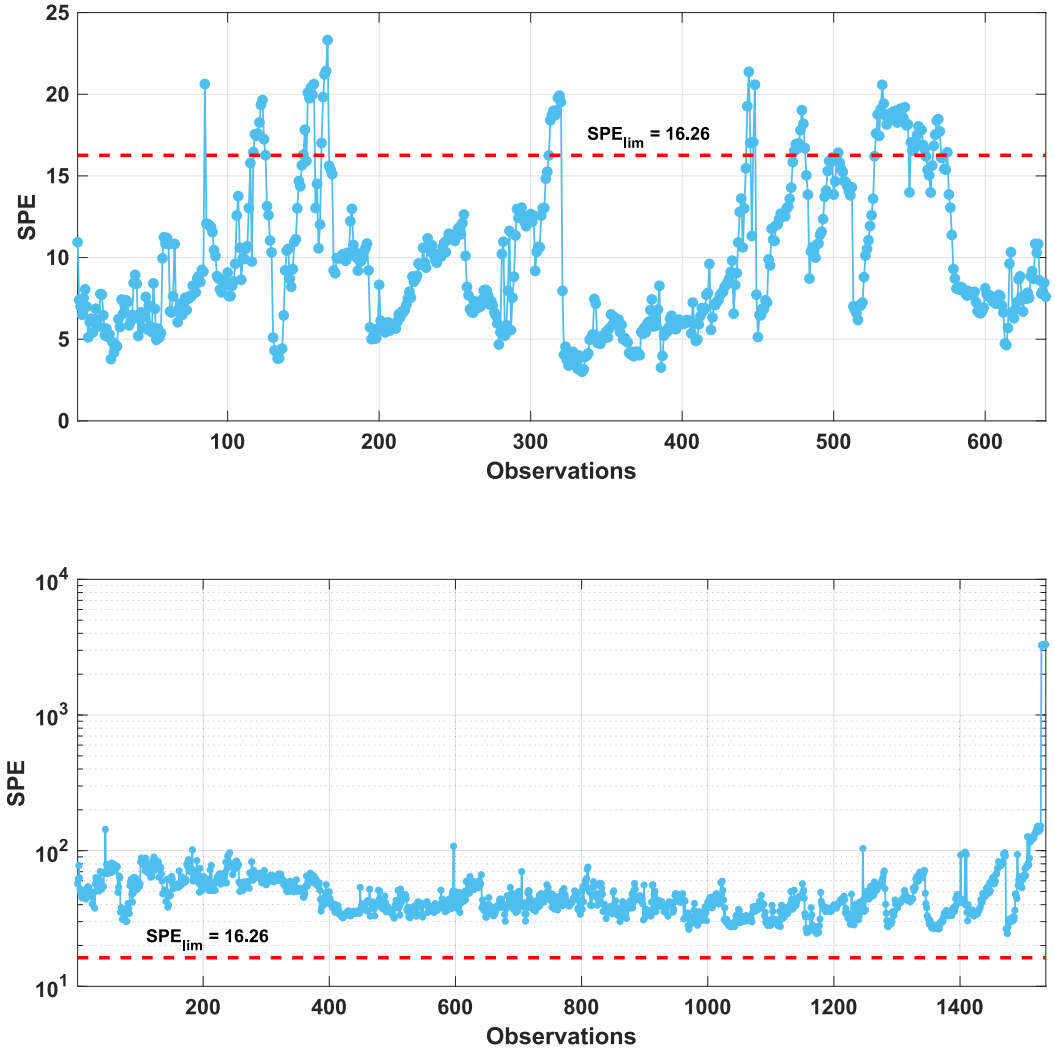

(a)

Fig. 7. Detection results for sinkhole event detection given probe (upper) and test (lower) using (a) PCA, and (b) VAE-CNN methods.

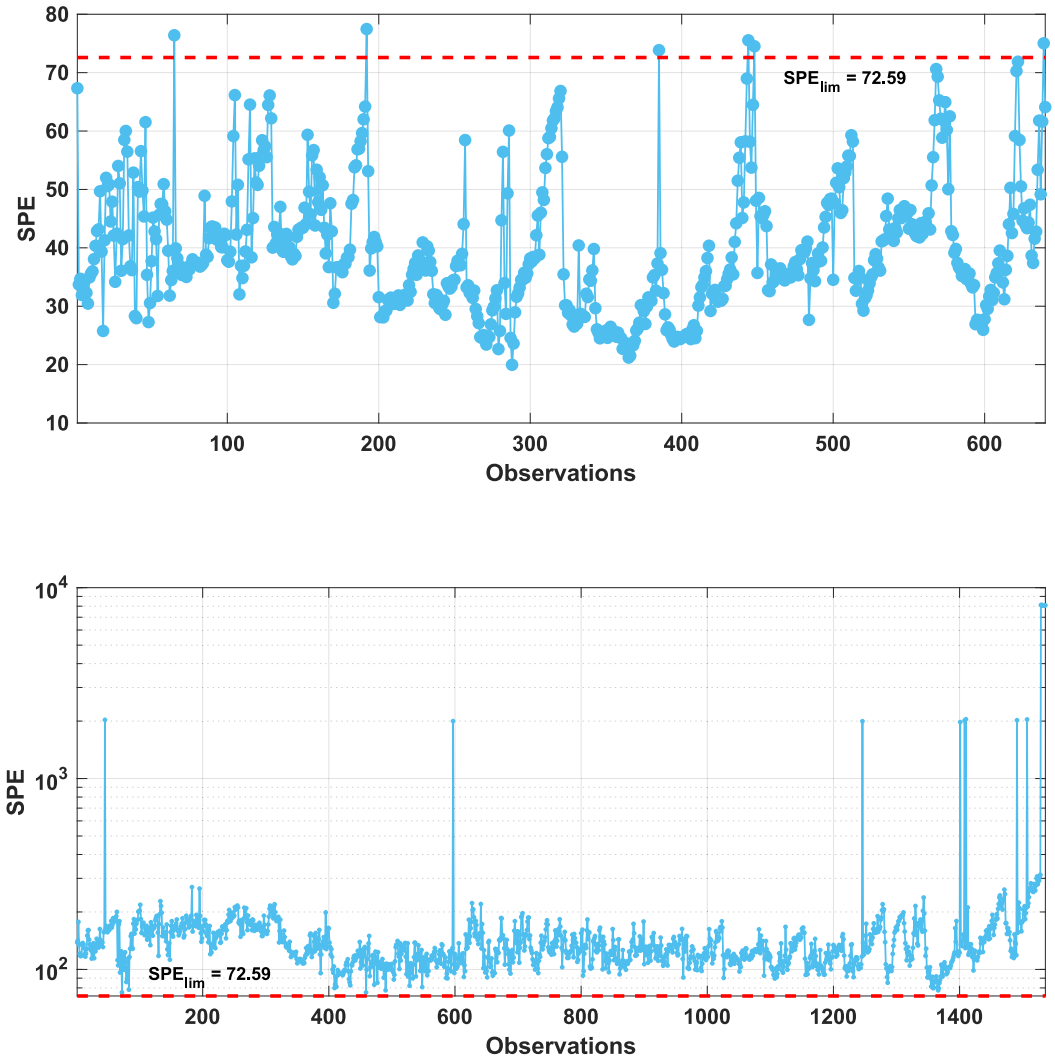

(b)

Fig. 7. (*continued*).

cutter teeth requiring more force, reducing the RPM. On the contrary, soft soils require less torque, allowing freer rotation of the cutter head and allowing high RPM.

4.2. Sinkhole event detection performance

The sinkhole event monitoring during the EPB operation involves propagating real-time sensor data to the corresponding trained model and computing the pertinent *SPE* for each observation, and comparing it with the defined control limit via KDE for each introduced method. This section describes the findings for detecting sinkhole events given by different methods. As the probe data consists of observations where sinkholes are not occurring, it is expected that all the *SPE* points fall below the control limit, while in the test set that is populated with observations where sinkhole occurrences are recorded, it is expected that all the *SPE* values fall over the limit, resulting in an alarm. Table 3 contains the performance metrics for the respective introduced methods divided into probe and test sets and their corresponding metrics to analyse the performance. Bold values in the table represent a superior performance over the introduced methods.

Fig. 7 shows the sinkhole event detection performance generated by the PCA and the introduced VAE-CNN methods, the SPE_{lim} is set to 16.26 and 72.59, respectively; moreover, the upper side corresponds to the probe test, while the lower side corresponds to the test set. Fig. 7**(a)** shows the SPE measurements computed for the probe set. It can be observed that several points surpass the control limit when they should be maintained below it, leading to a 12.8 % *FAR*, representing 82 false detected operational time instances. On the other hand, the detection performance for the test set successfully detected 98.8 % of the sinkhole events that occurred during the EPB operation. Fig. 7**(b)** depicts the detection performance for the proposed VAE-CNN method, in which the monitoring process for the probe dataset yields a total of six false alarms, representing 0.9 % of the total observations while successfully detecting the sinkhole occurrences in the test set.

These two methods were included in the results to discuss their effectiveness based on the data characteristics. The detection performance charts for the additional methods, including ICA, DICA, KPCA, AE, StackedAE and VAE, are illustrated in **Fig. S1** of the **SI**. According to the performance of both PCA and VAE-CNN methods, detecting anomalies during the monitoring of sinkhole events yielded a 98.8 % and 100 % detection rate. This is not the case for the AE and VAE, which yielded misdetection in values of 0.8 % and 0.9 %, respectively.

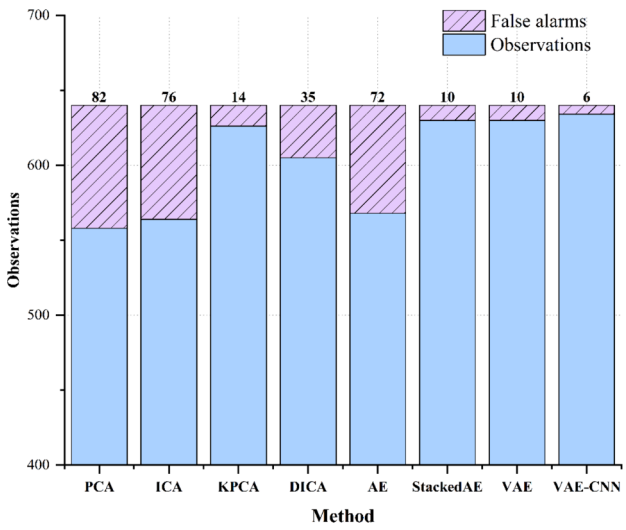

Fig. 8. False alarm instances during the sinkhole monitoring with the probe dataset.

The performances of these methods are closely related to the features included in their methods. For instance, PCA and ICA work with linear transformations that might fail when reconstructing the training observations properly, given the nonlinear nature of the EPB process data. This leads to drawbacks in the misdetection of abnormal events and the generation of false alarms. The *FAR* values yielded by PCA and ICA are 12.8 % and 11.9 %, respectively. In contrast, by including features such as non-linearity, adding kernel-based non-linear transformations, and considering temporal correlations by adding dynamicity, as with the KPCA and DICA, superior performances can be achieved. These methods succeed in detecting abnormal sinkhole occurrences and decreasing false alarms, as evidenced by *FAR* values of 2.3 % and 5.5 %, respectively.

For the neural methods, the lowest performance is yielded by the AE, corresponding to a single hidden layer with 13 neurons. As a non-linear variation of PCA, the activation function defines the transitions between layers to generate the hidden representation subspace. However, temporal correlations are not considered, resulting in poor performance with a misdetection rate of 0.8 % and a considerable *FAR* of 11.3 %. Similar issues arise with the StackedAE and VAE methods, which could generate reliable approximations to decrease false alarm generation. However, VAE did not completely detect all sinkhole occurrences. In contrast, the introduced VAE-CNN method achieved complete detection of sinkhole events while generating the lowest false alarms, with a 0 % misdetection rate and 0.9 % false alarm rate.

During the monitoring for sinkhole occurrences, false alarm generation plays a pivotal role in operational implications, with the most significant being the disruption of normal EPB construction. Unnecessary interventions lead to downtimes, affecting productivity and causing construction delays. Fig. 8 shows the false alarms yielded by each monitoring method, with PCA, ICA, and AE producing the highest false alarms at 82, 76, and 72 alarms, respectively. Considering that the observations have a time resolution of approximately 3 min, a total disruption between 4.1 and 3.6 h can be generated based on the total measurements. The implications of disruption are also financial, as managing false alarms generates costs for site investigation and increased workload that can become significant over time, potentially damaging the overall project budget. In this context, the lowest false alarms were triggered by the proposed VAE-CNN method, with a total of six false alarms representing less than 1 % of the project time analyzed interval. This indicates that it is an acceptable approach for generating reliable detections compared with state-of-the-art methods.

4.3. Sinkhole occurrence feature isolation

Once sinkhole events are detected in PM frameworks, the responsible sensor for the failure is isolated. Unlike those frameworks, the sinkhole occurrence event cannot be attributed to a sensor because they only measure operational observations from the EPB during excavation. Nevertheless, sinkhole formation is heavily related to unstable geological conditions in which some EPB operational variables play an important role in the excavation surroundings. The selected method for sensor isolation involves computing the *SVI* values that quantify the rate of *SPE* for each sensor over the overall *SPE*. This approach observes important features that can serve as indicators or related variables, allowing operators to receive an early warning when a sinkhole is about to occur and identify how these measurements are related to sinkhole occurrences.

Fig. 9 depicts the *SVI* computation counts generated during the monitoring of the test dataset, where sinkhole events are observed. The control limit for the *SVI* is 0.5, and when a measurement falls below this threshold, it is considered that this sensor contributes to the failure, serving as a variable that can indicate anomalies during the EPB operation. Important counts for the SVI falling below the control limit can be observed in features like the cutter RPM. In heterogeneous geologies, a high RPM can generate unstable ground conditions and consequently contribute to sinkhole formation.

In addition, the bottom earth pressure variable accounts for several

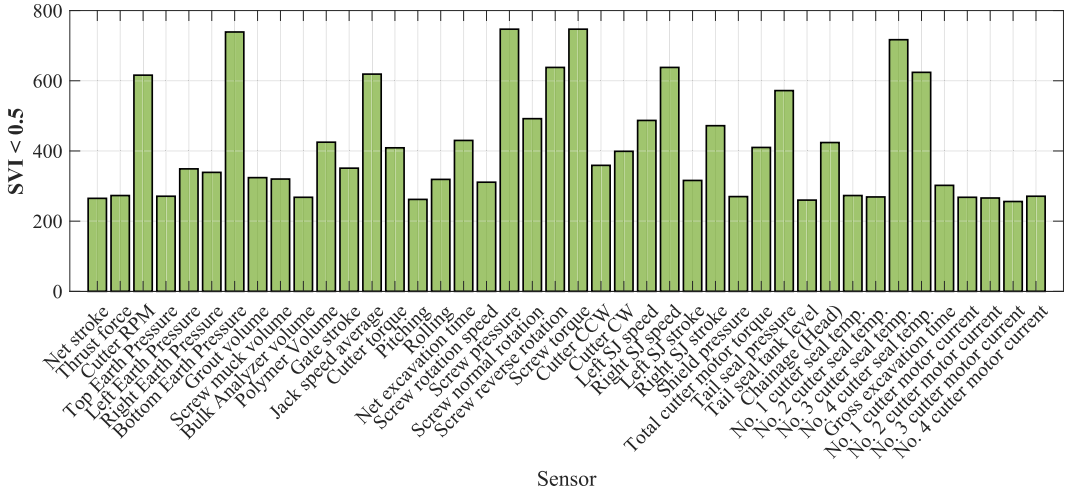

Fig. 9. SVI counts for the different EPB operational variables during the monitoring of the test data.

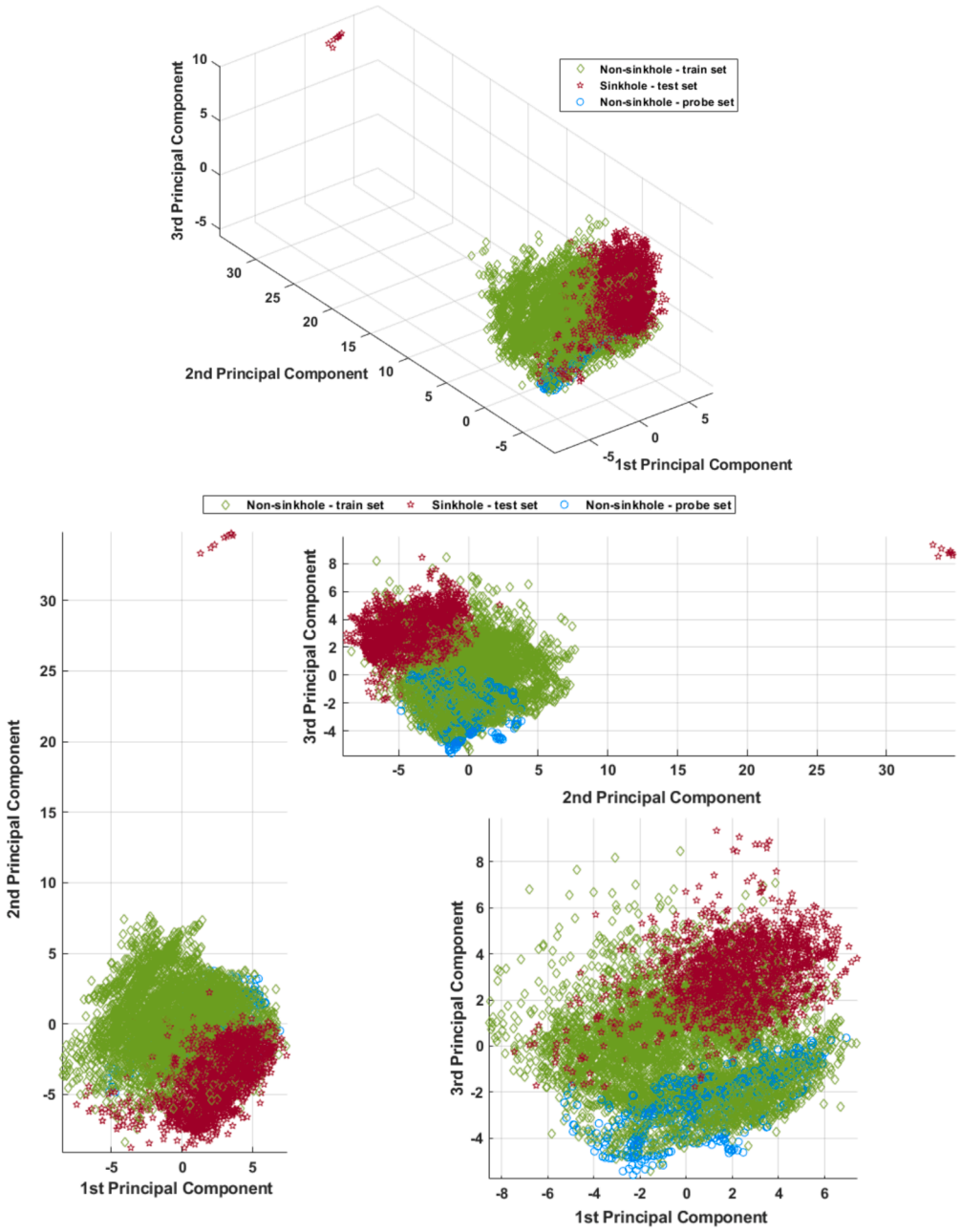

(a)

Fig. 10. Visualization of different components given the transformation via (a) PCA, and (b) t-SNE of introduced method residuals.

violations of the SVI control limit. The relationship between sinkhole formation and this feature is complex and context-dependent. For instance, EPB TBMs balance the pressure at the tunnel face with its surroundings,and when encountering hard rock geological conditions, the EPB may not achieve such balance. Moreover, the next observed feature with high *SVI* counting is the jack speed, which is highly related to the advanced rate. As the main cause of sinkhole formation is ground stability, rapid excavation leads to an increase in ground stress and consequent over excavation, which are major contributors to sinkhole formation.

Screw pressure, on the other hand, is a EPB operational variable that influences the behavior of the surrounding ground. With excessive screw pressure, the ground is disturbed, evidencing over-excavation, especially in soft geological conditions. However, screw reverse rotation, applied during EPB retraction, can be indirectly related to sinkhole formation because this variable influences the removal of excavated material rather than directly affecting ground stability. Excessive screw torque signifies high efficiency, which can increase ground disturbance in soft geology.

Finally, the cutter seal temperatures show a higher *SVI* count, in which temperature changes might affect the EPB performance and the ground. The cutter sealing element prevents the entry of soil, water and debris into the cutter head and prevents excessive wear. The sealing temperature indicates the condition and efficiency of the cutters. A

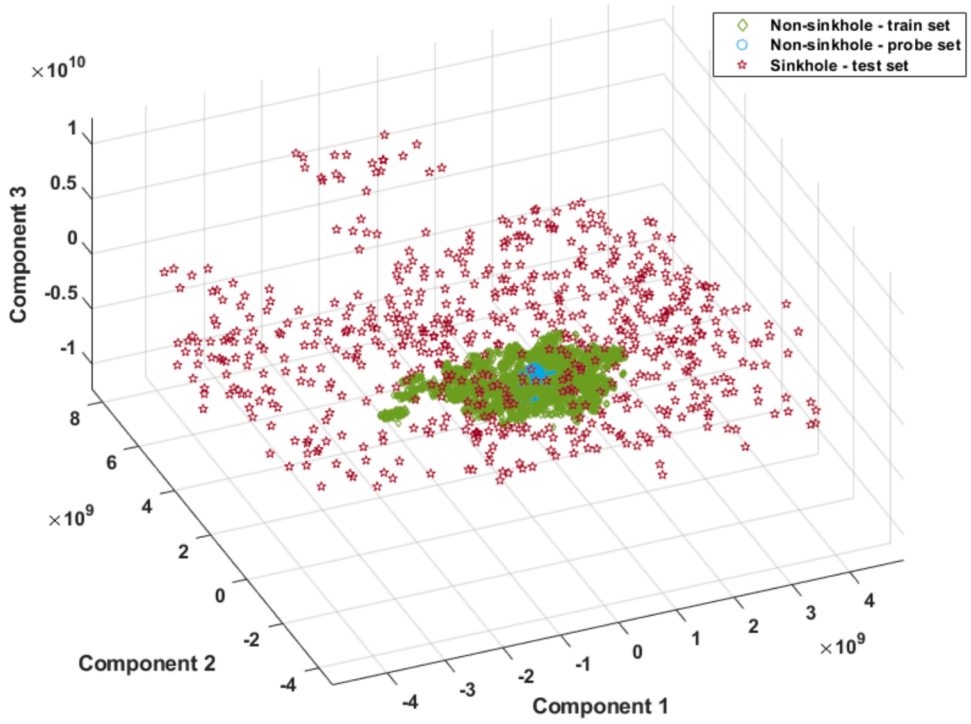

Fig. 10. (*continued*).

change in this temperature can be associated with water ingress into the tunneling area, affecting the ground stability as there could be changes in soil properties, increasing the risk of sinkhole formation (Fu et al., 2021; Janc et al., 2024).

An additional analysis involves visual aid from the feature extraction method, as it can visualize in three dimensions whether different conditions exist in the process data. Fig. 10**(a)** presents a scatter plot for the three principal components with different markers. In the different profiles, it can be observed that the three different conditions, i.e., the train, probe and test sets generate a defined cluster, making it difficult to diagnose sinkhole events during EPB excavation, reflecting the false alarm generation and in some cases, misdetecting the sinkhole conditions, demonstrating some difficulties when managing the dynamic and non-linear EPB feature signals.

In contrast, Fig. 10**(b)** shows the t-SNE transformation using the residual values from the reconstruction of the introduced VAE-CNN method. It can be observed that contrary to the PCA visualization, the conditions of the data are differentiated into clusters. Here, the train and probe datasets are clustered because the distribution of operational data is similar, with the probe dataset encapsulated within the train set. On the other hand, the test dataset, characterized by operational data with sinkhole occurrences, is differentiated from the other conditions. This is mainly due to the introduced features of the VAE-CNN method and its effective learning process to reconstruct non-linear and dynamic data.

4.4. *Practical implications of EPB-induced sinkhole monitoring*

Real-time monitoring of sinkhole occurrences during EPB operation is necessary to preserve the safety of workers, equipment, and surrounding infrastructure health, promptly detect sinkhole occurrences, and deploy mitigation measures. Nevertheless, there are challenges and limitations associated with deployments on a real-time EPB excavation, addressed as follows:

- *Data and resource availability:* Deploying a real-time monitoring system signifies computational power and storage limitations, especially when scaling up the trained models to handle large datasets while operating in a remote environment.
- *Operational pluralism:* Plural conditions during the excavation and long-term operations, including EPB machine properties, environmental conditions, geological factors, and operators' expertise, might affect the model performance and ability to generalize.
- *Model retraining:* Managing model drifting due to changes in operational and external factors of the excavation consists of continual retraining to adapt to the new conditions and maintain a reliable detection performance.

Deploying computational models on real engineering projects raises factors that consider the framework generalization across different geological settings and EPB or TBM types. Ideally, easy-to-adapt or universal models are required to overcome these necessities, as methods such as transfer learning are beneficial and will emerge as potential research paths in the future. Transfer learning techniques utilize knowledge across domains represented as EPB operational regimes under different conditions, resulting as well in a computationally efficient fashion that includes pre-trained models, domain adaptation, multitask learning, cross-lingual transfer learning, and progressive neural networks (Panigrahi et al., 2021).

Despite the abovementioned challenges, the proposed method demonstrated adequate robustness to digest high data volumes with non-linear and time-dependent characteristics. Collecting additional observations during the EPB operation allows the identification of condition changes and pertinent retraining to accommodate the new conditions, as well as addressing resources in computational requirements and pluralism management.

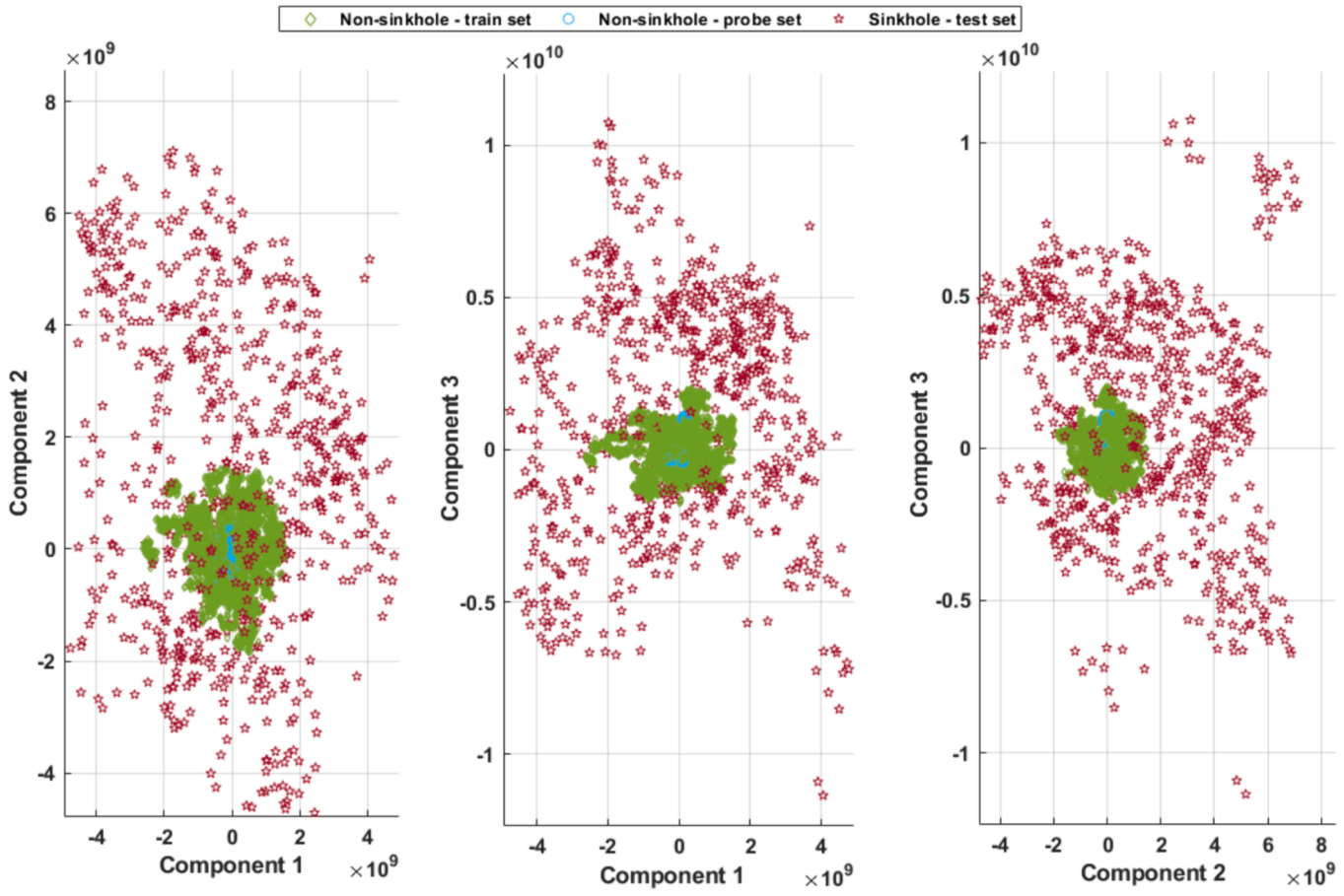

(b)

Fig. 10. (*continued*).

5. Conclusions

A real-time unsupervised monitoring framework for sinkhole formation occurrence via a coupled VAE-CNN method was developed to manage the behavior of multivariate EPB data in terms of non-linearity and temporal dependencies. The framework is divided into two main phases: *offline modeling*, where a data-intensive method is driven by training a feature extraction model to define a subspace in which representations define the behavior of multivariate data when a sinkhole formation does not occur. Then, *SPE* values are collected and generated by a control limit via *KDE*, which is used to determine whether unseen and operational EPB data correspond to a sinkhole formation. On the other hand, the *online monitoring* phase validates the trained feature extraction model when detecting sinkhole formation events. This unseen operational EPB data is propagated through the trained model and the computed *SPE* statistic is compared with the defined control limit. Different metrics are then utilized to assess the detection performance. After detection, feature isolation is conducted via *SVI* counts to determine the most important variables, discussing the relationship between higher counts of the variables *SVI* and sinkhole formation. Finally, visual aids with different methods, such as PCA and t-SNE transformation, are compared in terms of showing different conditions of the operational data.

The findings of this study are listed as follows:

- Several methods, including PCA, ICA, DICA, KPCA, AE, StackedAE, and VAE, were considered for monitoring sinkhole formation during EPB excavation. The proposed VAE-CNN method exhibited superiority, achieving 100 % and 0.9 % of *DR* and *FAR*, respectively.
- The proposed VAE-CNN-based monitoring resulted in a combination of models can manage non-linear and temporal dependencies evidenced by the operational data of the EPB excavation in normal conditions and non-sinkhole formations.
- Operationally, real-time identification of relevant variables during the detection of a sinkhole formation indicated a valuable tool for operators to recognize the risk and deploy pertinent protocols. Variables such as the cutter RPM and torque, jack speed, screw pressure, and sealing components were identified as indicators for possible sinkhole occurrences, considering their influence on ground stability.
- Visual tools derived from PCA and t-SNE allowed for the differentiation the conditions of the EPB operational variables, grouping the instances according to whether a sinkhole formation is occurring. The proposed method's effective reconstruction enabled the identification of these events in the form of clusters.

The proposed monitoring system deployed early warnings of potential sinkhole occurrences during EPB operation, enabling proactive planning to prevemt these events or the prompt implementation of emergency protocols.

CRediT authorship contribution statement

Jorge Loy-Benitez: Writing – original draft, Visualization, Validation, Software, Methodology, Investigation, Formal analysis, Data curation, Conceptualization. **Hyun-Koo Lee:** Validation, Investigation, Formal analysis, Data curation, Conceptualization. **Myung Kyu Song:** Writing – review & editing, Formal analysis, Conceptualization. **Je-Kyum Lee:** Formal analysis, Data curation. **Sean Seungwon Lee:** Writing – review & editing, Resources, Project administration, Funding acquisition, Conceptualization.

Declaration of competing interest

The authors declare that they have no known competing financial interests or personal relationships that could have appeared to influence the work reported in this paper.

Data availability

Data will be made available on request.

Acknowledgments

This work was supported by the Korea Agency for Infrastructure Technology Advancement (KAIA) grant funded by the Ministry of Land, Infrastructure and Transport (Grant No. RS-2020-KA157786) and the BK21 FOUR (Fostering Outstanding Universities for Research) program (No. 4299990314624) through the National Research Foundation of Korea (NRF) funded by the Korea Ministry of Education.

Appendix A. Supplementary data

Supplementary data to this article can be found online at https://doi.org/10.1016/j.tust.2024.105908.

References

Attewell, P.B., Yeates, J., Selby, A.R., 1986. Soil movements induced by tunnelling and their effects on pipelines and structures. Blackie, New York.

Ayawah, P.E.A., Sebbeh-Newton, S., Azure, J.W.A., Kaba, A.G.A., Anani, A., Bansah, S., Zabidi, H., 2022. A review and case study of Artificial intelligence and Machine learning methods used for ground condition prediction ahead of tunnel boring Machines. Tunn. Undergr. Sp. Technol. 125, 104497 https://doi.org/10.1016/j.tust.2022.104497.

Ba-Alawi, A.H., Vilela, P., Loy-Benitez, J., Heo, S.K., Yoo, C.K., 2021. Intelligent sensor validation for sustainable influent quality monitoring in wastewater treatment plants using stacked denoising autoencoders. J. Water Process Eng. 43, 102206 https://doi.org/10.1016/j.jwpe.2021.102206.

Bai, S., Kolter, J.Z., Koltun, V., 2018. An Empirical Evaluation of Generic Convolutional and Recurrent Networks for Sequence Modeling.

Brooks, S.K., Bauer, M., 2018. Sensor validation and reconstruction: Experiences with commercial technology. Control Eng. Pract. 77, 28–40. https://doi.org/10.1016/J.CONENGPRAC.2018.04.003.

Chen, X.J., Fang, P.P., Chen, Q.N., Hu, J., Yao, K., Liu, Y., 2024. Influence of cutterhead opening ratio on soil arching effect and face stability during tunnelling through non-uniform soils. Undergr. Sp. 17, 45–59. https://doi.org/10.1016/j.undsp.2023.11.003.

Chen, X., Hu, Y., Zhang, L., Liu, Y., 2023. 3D large-deformation modelling on face instability and sinkhole formation during tunnelling through non-uniform soils. Tunn. Undergr. Sp. Technol. 134, 105011 https://doi.org/10.1016/j.tust.2023.105011.

Chen, R., Zhang, P., Wu, H., Wang, Z., Zhong, Z., 2019. Prediction of shield tunneling-induced ground settlement using machine learning techniques. Front. Struct. Civ. Eng. 13, 1363–1378. https://doi.org/10.1007/s11709-019-0561-3.

Fang, K., Yang, Z., Jiang, Y., Sun, Z., Wang, Z., 2020. Surface subsidence characteristics of fully overlapping tunnels constructed using tunnel boring machine in a clay stratum. Comput. Geotech. 125, 103679 https://doi.org/10.1016/j.compgeo.2020.103679.

Fu, J., Xia, Y., Lan, H., Wu, D., Lin, L., 2021. A case study on TBM cutterhead temperature monitoring and mud cake formation discrimination method. Sci. Rep. 11, 1–12. https://doi.org/10.1038/s41598-021-99439-x.

Gondara, L., Wang, K., 2018. MIDA: Multiple imputation using denoising autoencoders. Lect. Notes Comput. Sci. (including Subser. Lect. Notes Artif. Intell. Lect. Notes Bioinformatics) 10939 LNAI, 260–272. https://doi.org/10.1007/978-3-319-93040-4_21.

Guo, D., Li, J., Li, X., Li, Z., Li, P., Chen, Z., 2022. Advance prediction of collapse for TBM tunneling using deep learning method. Eng. Geol. 299 https://doi.org/10.1016/j.enggeo.2022.106556.

Guo, F., Xie, R., Huang, B., 2020. A deep learning just-in-time modeling approach for soft sensor based on variational autoencoder. Chemom. Intell. Lab. Syst. 197, 103922 https://doi.org/10.1016/J.CHEMOLAB.2019.103922.

Heloulou, N., Ramdani, M., 2014. Robust Statistical Process Monitoring for Biological Nutrient Removal Plants. Commun. Comput. Inf. Sci. 442 CCIS, 427–436. https://doi.org/10.1515/teme-2018-0037.

Hernán, D.M., Córdova, F.M., Cañete, L., Palominos, F., Cifuentes, F., Sánchez, C., Herrera, M., 2015. Order and chaos in the brain: Fractal time series analysis of the EEG activity during a cognitive problem solving task. Procedia Comput. Sci. 55, 1410–1419. https://doi.org/10.1016/j.procs.2015.07.135.

Huang, X., Zhang, Q., Liu, Q., Liu, X., Liu, B., Wang, J., Yin, X., 2022. A real-time prediction method for tunnel boring machine cutter-head torque using bidirectional long short-term memory networks optimized by multi-algorithm. J. Rock Mech. Geotech. Eng. 14, 798–812. https://doi.org/10.1016/j.jrmge.2021.11.008.

Janc, B., Vižintin, G., Pal, A., 2024. Investigation of Disc Cutter Wear in Tunnel-Boring Machines (TBMs): Integration of Photogrammetry, Measurement with a Caliper, Weighing, and Macroscopic Visual Inspection. Appl. Sci. 14, 2443. https://doi.org/10.3390/app14062443.

Kalchbrenner, N., Grefenstette, E., Blunsom, P., 2014. A convolutional neural network for modelling sentences. 52nd Annu. Meet. Assoc. Comput. Linguist. ACL 2014 - Proc. Conf. 1, 655–665. https://doi.org/10.3115/v1/p14-1062.

Kim, M., Liu, H., Kim, J.T., Yoo, C., 2013. Sensor fault identification and reconstruction of indoor air quality (IAQ) data using a multivariate non-Gaussian model in underground building space. Energy Build. 66, 384–394. https://doi.org/10.1016/j.enbuild.2013.07.002.

Kingma, D.P., Welling, M., 2019. An introduction to variational autoencoders. Found. Trends Mach. Learn. 12, 307–392. https://doi.org/10.1561/2200000056.

Ko, T.Y., Lee, S.S., 2020. Effect of rock abrasiveness on wear of shield tunnelling in Bukit Timah granite. Appl. Sci. 10 https://doi.org/10.3390/app10093231.

Ku, W., Storer, R.H., Georgakis, C., 1995. Disturbance detection and isolation by dynamic principal component analysis. Chemom. Intell. Lab. Syst. 30, 179–196. https://doi.org/10.1016/0169-7439(95)00076-3.

Lee, S., Kwak, M., Tsui, K.-L., Kim, S.B., 2019. Process monitoring using variational autoencoder for high-dimensional nonlinear processes. Eng. Appl. Artif. Intell. 83, 13–27. https://doi.org/10.1016/J.ENGAPPAI.2019.04.013.

Lee, H.K., Song, M.K., Seungwon Lee, S., 2021. Prediction of subsidence during tbm operation in mixed-face ground conditions from realtime monitoring data. Appl. Sci. 11 https://doi.org/10.3390/app112412130.

Lee, J.M., Yoo, C.K., Lee, I.B., 2004. Statistical process monitoring with independent component analysis. J. Process Control 14, 467–485. https://doi.org/10.1016/j.jprocont.2003.09.004.

Liu, H., Zhou, J., Xu, Y., Zheng, Y., Peng, X., Jiang, W., 2018. Unsupervised fault diagnosis of rolling bearings using a deep neural network based on generative adversarial networks. Neurocomputing. https://doi.org/10.1016/J.NEUCOM.2018.07.034.

Lotfalinezhad, H., Maleki, A., 2020. TTA, a new approach to estimate Hurst exponent with less estimation error and computational time. Phys. A Stat. Mech. Its Appl. 124093 https://doi.org/10.1016/J.PHYSA.2019.124093.

Loy-Benitez, J., Tariq, S., Tra, H., Heo, S., Yoo, C., 2023. Sludge bulking monitoring in industrial wastewater treatment plants through graphical methods: A dynamic graph embedding and Bayesian networks approach. J. Environ. Manage. 345, 118804 https://doi.org/10.1016/j.jenvman.2023.118804.

Loy-Benitez, J., Kyu, M., Choi, Y., Lee, J., Seungwon, S., 2024a. Breaking new ground: Opportunities and challenges in tunnel boring machine operations with integrated management systems and artificial intelligence. Autom. Constr. 158, 105199 https://doi.org/10.1016/j.autcon.2023.105199.

Loy-Benitez, J., Lee, H., Kyu, M., Choi, Y., Seungwon, S., 2024b. Transfer component analysis-driven domain adaptation approach for estimating the life of tunnel boring machine disc cutters. Tunn. Undergr. Sp. Technol. Inc., Trenchless Technol. Res. 147, 105714 https://doi.org/10.1016/j.tust.2024.105714.

Mandelbrot, B.B., Wallis, J.R., 1969. Robustness of the rescaled range R/S in the measurement of noncyclic long run statistical dependence. Water Resour. Res. 5, 967–988. https://doi.org/10.1029/WR005i005p00967.

Navi, M., Meskin, N., Davoodi, M., 2018. Sensor fault detection and isolation of an industrial gas turbine using partial adaptive KPCA. J. Process Control 64, 37–48. https://doi.org/10.1016/j.jprocont.2018.02.002.

Panigrahi, S., Nanda, A., Swarnkar, T., 2021. A Survey on Transfer Learning. Smart Innov. Syst. Technol. 194, 781–789. https://doi.org/10.1007/978-981-15-5971-6_83.

Peck, R.B., 1969. Deep excavation and tunnelling in soft ground. Proceed. 7th Int. Conf. Soil Mech. Found. Eng. 225–290.

Pourhashemi, S.M., Ahangari, K., Hassanpour, J., Eftekhari, S.M., 2022. TBM performance analysis in very strong and massive rocks; case study: Kerman water conveyance tunnel project. Iran. Geomech. Geoengin. 17, 1110–1122. https://doi.org/10.1080/17486025.2021.1912410.

Qiao, W., Huang, X., 2022. How does transportation development affect environmental performance? Evidence from Hainan Province. China. Cities 129, 103835. https://doi.org/10.1016/j.cities.2022.103835.

Rumelhart, D.E., Hintont, G.E., 2019. Learning Representations by Back-Propagating Errors. Cogn. Model. 3–6 https://doi.org/10.7551/mitpress/1888.003.0013.

van der Maaten, L., Hinton, G., 2008. Visualizing Data using t-SNE Laurens. J. Mach. Learn. Res. 9, 2579–2605. https://doi.org/10.1007/s10479-011-0841-3.

Wan, Z., Li, S., Zhao, S., Liu, R., 2024. Rheological characterization of the conditioned sandy soil under gas-loading pressure for earth pressure balance shield tunnelling. Tunn. Undergr. Sp. Technol. 146, 105658 https://doi.org/10.1016/j.tust.2024.105658.

Wang, S., Chen, Y., 2004. Sensor validation and reconstruction for building central chilling systems based on principal component analysis. Energy Convers. Manag. 45, 673–695. https://doi.org/10.1016/S0196-8904(03)00180-8.

Wang, H., Wang, J., 2020. The multi-objective optimization of tunneling boring machine control based on geological conditions identification. J. Intell. Manuf. Spec. Equip. 1, 87–105. https://doi.org/10.1108/jimse-07-2020-0005.

Yan, W., Guo, P., Gong, L., Li, Z., 2016. Nonlinear and robust statistical process monitoring based on variant autoencoders. Chemom. Intell. Lab. Syst. 158, 31–40. https://doi.org/10.1016/J.CHEMOLAB.2016.08.007.

Zhang, Z., Jiang, T., Zhan, C., Yang, Y., 2019. Gaussian feature learning based on variational autoencoder for improving nonlinear process monitoring. J. Process Control 75, 136–155. https://doi.org/10.1016/J.JPROCONT.2019.01.008.

Zhou, J., Shi, X., Du, K., Qiu, X., Li, X., Mitri, H.S., 2017. Feasibility of random-forest approach for prediction of ground settlements induced by the construction of a shield-driven tunnel. Int. J. Geomech. 17 https://doi.org/10.1061/(asce)gm.1943-5622.0000817.